Comparison of OVERFLOW Computational and Experimental Results of the CobraMRV Mars Entry Vehicle Concept during Supersonic Retropropulsion

Kristen V. Matsuno*, Robert E. Childs†, Thomas H. Pulliam‡, Paul M. Stremel§ Patrick J. Moran¶, and Joseph A. Garcia‖
NASA Ames Research Center, Moffett Field, California 94305

The CFD solver OVERFLOW was used to simulate the CobraMRV undergoing supersonic retropropulsion (SRP) in the Langley Unitary Plan Wind Tunnel as part of a CFD and wind-tunnel integration effort. The aerodynamics of the CobraMRV are summarized and selected comparisons to experimental data at flight conditions are presented. The sensitivity of vehicle loads and flow field unsteadiness to CFD parameters at a subset of operating conditions are investigated.

Nomenclature

MRV	=	Mid-Lift/Drag Rigid Vehicle
HIAD	=	Hypersonic Inflatable Aerodynamic Decelerator
CFD	=	computational fluid dynamics
SRP	=	supersonic retropropulsion
RANS	=	Reynolds-Averaged Navier-Stokes
DES	=	Detached eddy simulation
SST	=	Shear stress transport
QCR	=	quadratic constitutive relation
CC	=	classical compressibility
RC	=	rotation and curvature correction
AMR	=	adaptive mesh refinement
PSP	=	pressure sensitive paint
CT	=	(engine) coefficient of thrust
M	=	Mach number
C_D	=	drag coefficient
C_L	=	lift coefficient
C_p	=	pressure coefficient
C_x	=	axial force coefficient
C_{mz}	=	rolling moment coefficient
α	=	model pitch (angle of attack, degrees)
β	=	model roll (degrees)
ϕ	=	model yaw (degrees)

I. Introduction

LANDING large payloads on the surface of Mars is one of the foremost technical challenges to manned exploration of our solar system. The tenuous Mars atmosphere limits the deceleration that can be achieved by traditional

*Aerospace Engineer, NASA Systems Analysis Office, AIAA Member
†Senior Research Scientist, Science & Technology Corporation
‡Senior Research Scientist, Science & Technology Corporation, AIAA Associate Fellow
§Senior Research Scientist, Science & Technology Corporation, AIAA Member
¶Computer Scientist, Advanced Computing Branch, NASA Ames Research Center
‖Aerospace Engineer, NASA Systems Analysis Office, AIAA Senior Member

aerodynamic drag, but is dense enough to create complex vehicle aerodynamics when retropropulsion is used. Recent NASA Rover missions have employed four stages of deceleration and landing technology: a conventional aeroshell, a super/subsonic parachute, retropropulsion and a sky-crane. This has proven to be a reliable approach, but it is complex and has distinct disadvantages for crewed missions. A critical future requirement is for a Mars lander vehicle that exhibits favorable drag characteristics and maneuverability [1, 2]. One such vehicle concept is the CobraMRV (Cobra Mid-Lift/Drag Rigid Vehicle). Figure 1 gives examples of the current vision for this vehicle. This concept is designed for traditional hypersonic aerodynamic drag and guidance through supersonic flight, down to $M \sim 2$, at which point supersonic retropropulsion (SRP) is used for final deceleration and landing. The engines are integrated into the vehicle and shielded for initial hypersonic entry, and the nozzle exit planes are exposed during SRP. Vehicles using SRP fly into the complex flow generated by the vehicle's plumes interacting with the freestream. The SRP rocket plumes exert a strong influence over the vehicle's aerodynamics and can cause negative vehicle aerodynamic drag (excluding rocket thrust) for some vehicle and nozzle combinations. Furthermore, because vehicle flights occur in the thin, mostly CO_2 Mars atmosphere, detailed aerodynamic data on such conditions are difficult to obtain. The ability of CFD to accurately predict both SRP aerodynamics for Mars is therefore crucial. This paper describes the use of OVERFLOW to predict the complex aerodynamics of the CobraMRV concept vehicle during SRP.

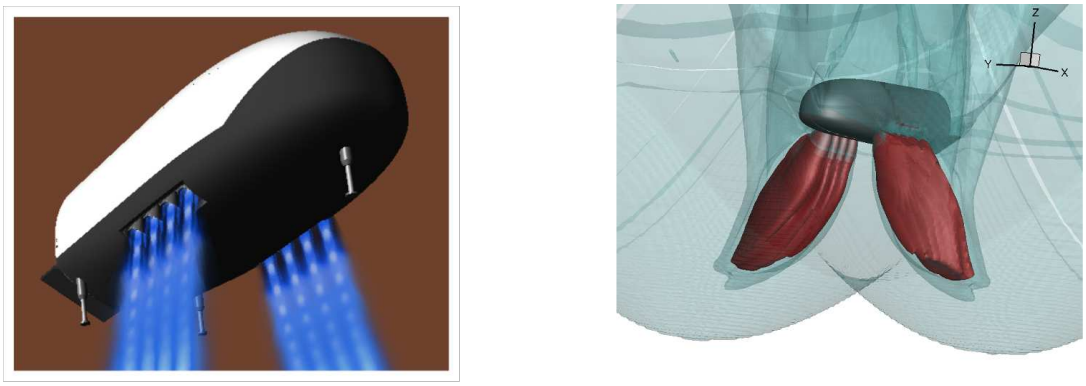

Fig. 1 The CobraMRV concept vehicle for landing large payloads on Mars; artistic render (left) and isosurfaces (right) showing the bow shock and plume structures.

A. Flow phenomena

An understanding of the dominant phenomena in SRP flows is necessary to grasp the challenges of SRP simulations. Several flow characteristics are dependent on the complex plume dynamics. Primarily, as the plumes jut out into the free stream, a bow shock with varying concavity and convexity takes shape. In high thrust configurations, this bow shock forward of the CobraMRV typically takes on a double-humped topology, as shown in Fig. 2. A portion of the bow shock situated between the two rows of plumes forms a nearly normal shock, also referred to as the "saddle" shock in this work. At the higher Mach numbers and thrust coefficients, this double-hump and saddle shock structure is much more pronounced. The difference in stagnation pressure losses through the oblique and normal regions of the steady or unsteady bow shock can be significant, leading to non-uniform flow stagnation pressure and entropy, regions of elevated vorticity, and increased surface pressures on the Cobra heatshield. Furthermore, depending on the turbulence model applied, this bow shock and plume structure can become highly unsteady, which further complicates flow field analysis.

B. Present objectives

This work uses OVERFLOW calculations and experimental data available from testing in the Langley Unitary Planform Wind Tunnel (UPWT) [3] to investigate the aerodynamic characteristics of the CobraMRV. A companion paper by Halstrom et al. [4] addresses the aerodynamics of an alternative Mars lander concept referred to as the HIAD (Hypersonic Inflatable Aerodynamic Decelerator) vehicle, using similar CFD methods and comparison metrics. Mean surface pressure distributions and trends from experimental data are discussed and compared to CFD for selected conditions. Unsteadiness in the flow field is compared and discussed in context of computational efficiency and cost. Cases with interesting flow features such as elevated unsteadiness, asymmetric loads, and outliers in CFD performance are investigated. A brief overview of the experimental data used in this work is given in the section below.

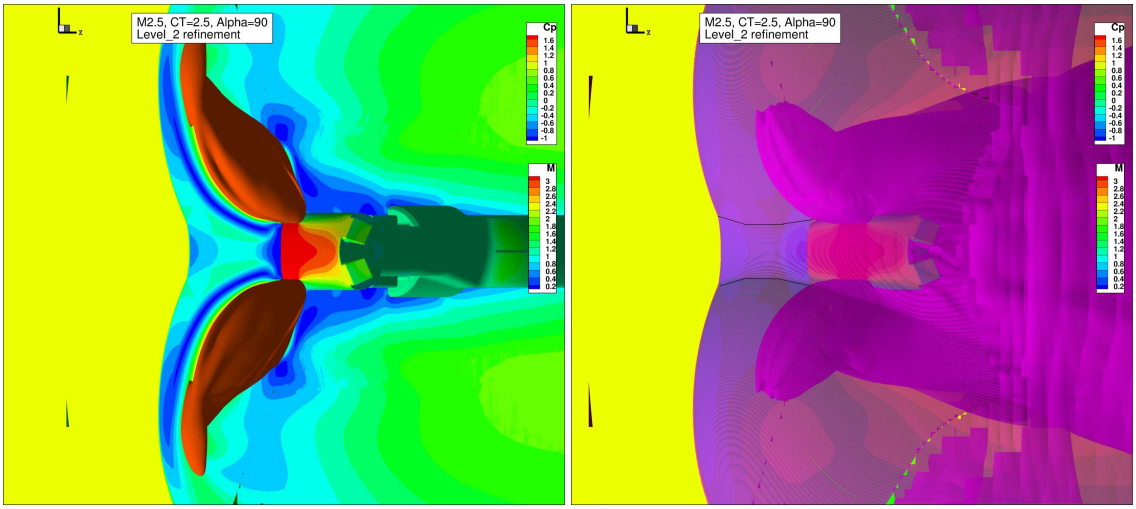

Fig. 2 Visualization of the plumes and bow shock of the CobraMRV at $M = 2.386, \alpha = 90°$ and $CT = 2.5$ from URANS calculations: (left) T_0 isosurfaces to demonstrate plume structures; (right) Mach number isosurface with black lines indicating the 'saddle' shock region. Heatshield colored by C_p.

C. Experimental data

Experimental details and metrics relevant to comparisons with CFD of the CobraMRV are given in this section. Further details on the overall experiment and the other testing configurations are available in a companion paper [3].

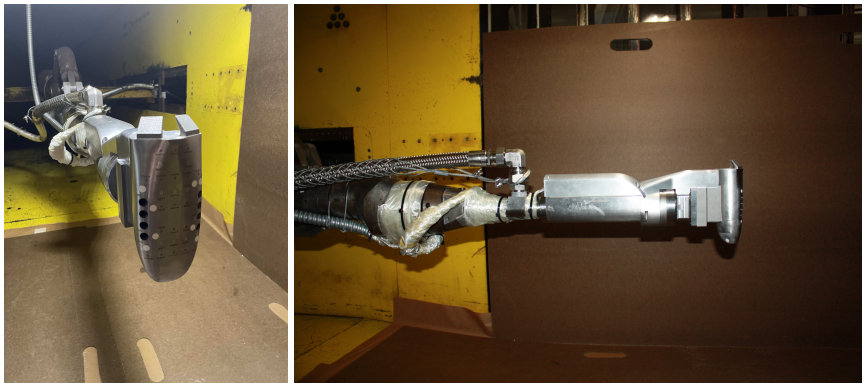

Fig. 3 Downstream and side views of the model CobraMRV as installed in test section 2 of the NASA Langley UPWT.

The six inch model CobraMRV wind tunnel model was mounted in test section 2 of the NASA Langley UPWT as shown in Fig. 3. The model was tested at Mach 2.4 and 3.5 with model pitches (angles of attack) ranging from $\alpha \in [80, 100]$, roll angles of $\beta \in [-10, 10]$ and model yaws ranging from $\phi \in [0, 180]$. The definition of these angles in the model coordinate system used throughout this paper are given in Fig. 4.

The jet thrust coeffients in this test varied from $CT \in [0.5, 2.5]$. The CobraMRV was not placed on a balance to compute the total thrust. Instead, the thrust was computed using the conditions in the jet plenum and *Gasprops* [5].

Four major types of experimental data are available for comparison to CFD of the CobraMRV: static pressure tap data, dynamic Kulite pressure data, pressure-sensitive paint (PSP) images, and Schlieren images.

Figure 5 shows the instrumentation locations on the heatshield of the CobraMRV; sensors on the perimeter of the heatshield, the backshell of the CobraMRV, and the support sting are not shown. Time-averaged pressures are available from the 29 static taps. Instantaneous pressures recorded at 20 kHz are available from the 14 Kulites. Mean coefficients of pressure, C_p, from the static taps and standard deviations of C_p from the Kulites are two of the main quantitative comparisons used from this experiment.

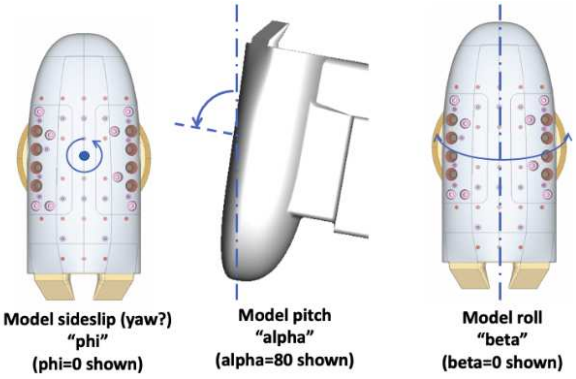

Fig. 4 Definition of angles specifying model configuration

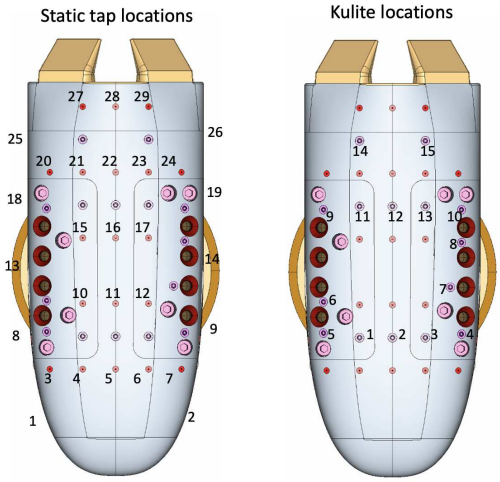

Fig. 5 Static tap and Kulite sensor locations on the CobraMRV model.

Visual datasets from the experiment are essential for qualitative comparisons to CFD and evaluation of off-surface flow features. Time-averaged C_p distributions on the heatshield are available from PSP images. Examples of PSP images at a special condition of interest are given with increasing CT in Fig. 8. High speed Schlieren movies provide visualizations of density variations in the flow field. Comparisons of numerical and experimental Schlieren images are particularly useful in showing the topography and unsteadiness of the bow shock.

II. CFD Methods

All simulation results were calculated using OVERFLOW, which solvers the Navier-Stokes equations on systems of overset grids. These numerical methods are further outlined in a companion paper [6], and will be briefly summarized in this section.

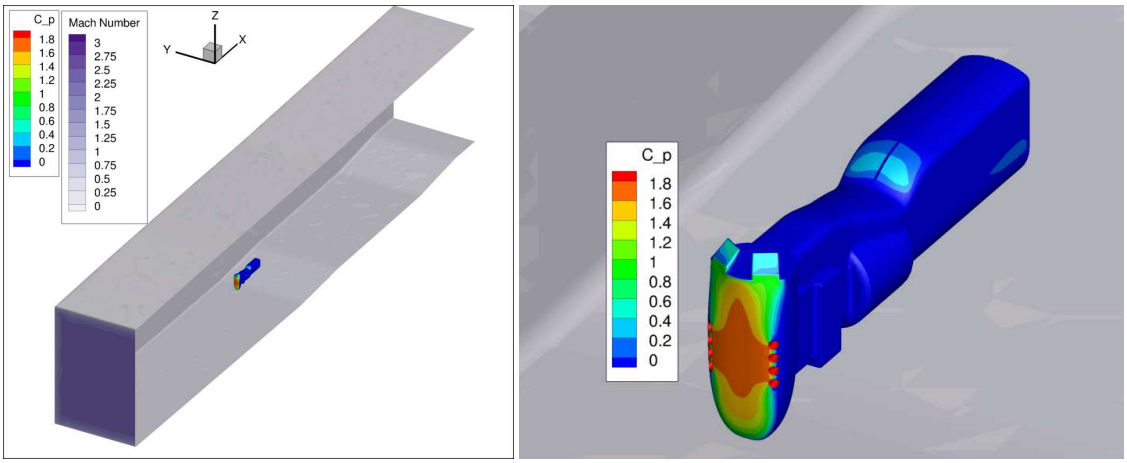

Fig. 6 Overview of computational domain and model geometry.

OVERFLOW's overset gridding capability allows different CFD parameters and methods to be applied in each grid of an overall grid system. Figure 6 shows the computational domain, model and truncated sting used in this work. Tunnel modelling and boundary conditions are identical to those used in pre-test work [7]. Present work applies the HLLC upwinding algorithm and van Albada limiter in the freestream and near body region. The HLLE++ upwinding algorithm and Koren limiter are locally applied in the shock and plume region for more robust shock capturing. Given the unsteady nature of the flow once sufficient grid resolution is used, simulations are run in time-accurate mode with BDF2 time integration and five subiterations. Pre-test CFD applied two levels of mesh adaption and dynamic adaptive mesh refinement (AMR) on individual shock and plume grids. Post-test CFD applied four levels of mesh adaption and dynamic AMR on a single grid encompassing the shock and plumes. The plume regions near the nozzle exits are limited to only three levels of adaption and the near-heatshield region are limited to only two levels of adaption in order to better distribute the adaption resources for other regions of the flow. In the final paper, the distinction between pre- and post-test cases needs will be further clarified.

The present work uses the SST model [8] in unsteady RANS (URANS), DES [9], and TMRC [10] calculations. The TMRC model incorporates both rotation and curvature (RC) and classic compressibility (CC) effects. URANS and DES calculations are run with other model modifiers to account for these effects. Throughout the domain, the model option for rotation and curvature (RC) [11] is enabled and the Suzen and Hoffman[12] 'compressibility correction' is disabled. The quadratic constitutive relation (QCR) modifier [13, 14] is enabled in wall-adjacent grids to enhance prediction of corner flow vortices, but is disabled in the test section core, the regions of the CobraMRV model, sting, plumes and bow shock.

III. Results

In this section, general trends in OVERFLOW calculations of the CobraMRV and comparisons to experimental data are summarized. The data available for evaluation of the mean flow field (static taps and PSP images) are discussed, followed by observations on data pertinent to flow field unsteadiness (Kulites and Schlieren images). The final paper

will include in-depth investigations into a few conditions of interest.

A. Mean surface pressures: static taps and PSP images

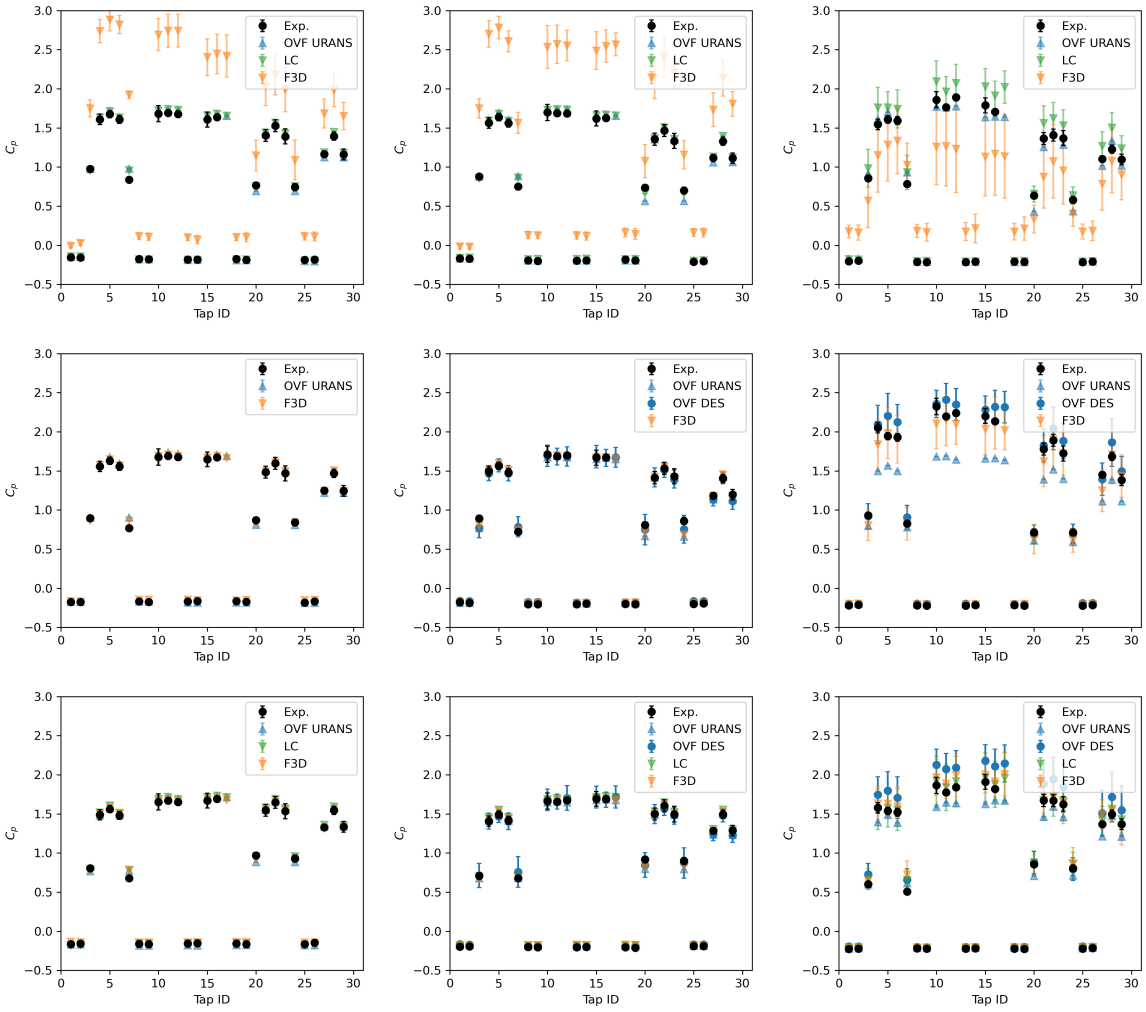

Fig. 7 Static tap C_p values at M=2.4, $\alpha = 80$ (top), $\alpha = 85$, and $\alpha = 90$ (bottom). From left to right: CT=[0.5, 1.0, 2.5]. All conditions are at $\beta = 0$, $\phi = 180$.

Static tap and pressure sensitive paint (PSP) measurements of C_p on the vehicle surface are a primary source of mean, quantitative data for comparison to CFD. In Fig. 7, the static tap C_p values are compared to pre-test values from OVERFLOW, Fun3D, and LociChem at several conditions. The values from the other CFD solvers are included to give context to the spread of CFD data compared to the data uncertainty. Note that static tap 17 was invalidated during experimental runs and excluded from these comparisons. It is important to distinguish that uncertainty bounds on experimental markers indicate the repeatability parameter. This parameter incorporates the variation due to the model type at all conditions and configurations, and is not specific to a particular CT, Mach number, or flight angles. The uncertainty bounds on CFD data points indicates the standard deviation due to unsteadiness in the flow solution for that specific CT, Mach and flight angle. While the repeatability parameter is not directly comparable to these standard deviations from CFD, it is included to indicate the uncertainty quantification of the static tap measurements as unsteady measurement at these points is unavailable.

Static tap mean C_p values generally match OVERFLOW URANS results well at lower CT values of 0.5 and 1. Pre-test OVERFLOW DES results are not available for all conditions. The effect of turbulence modelling is discussed in section III.C below. Higher CT cases show more variation in mean and fluctuating C_p values from both the experimental

and CFD measurements. We also observe more agreement with the experimental data in static taps' mean C_p and kulites' standard deviation of C_p for DES compared to URANS. This difference is discussed further in subsection III.C.

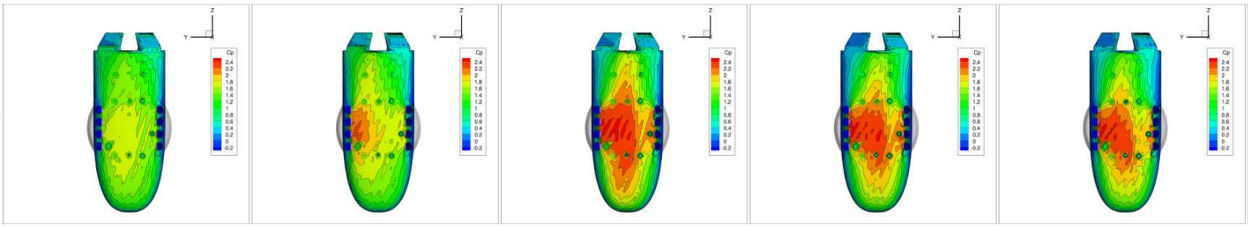

Fig. 8 Effects of increasing CT on PSP C_p contours of the CobraMRV heatshield at $M = 2.4, \alpha = 80, \beta = -5, \phi = 153.4$ at (left to right) $CT = [0.5, 1.0, 1.5, 2.0, 2.5]$.

PSP images provide an average view of C_p distributions on the surface of the CobraMRV. High temperatures during testing and image acquisition noise presented several data processing challenges, and resulting PSP C_p contours were dependent on anchoring using static tap values. At Kulite locations, PSP data is irregular due to local heating. Details on PSP acquisition and processing will be included in a companion paper [3]. Raw PSP images include vertical striping artifacts, but are still useful comparisons to CFD data. Fig 8 shows the effect of increasing CT on raw PSP C_p contours. Banding artifacts are visible at all conditions, and a region of higher C_p is biased towards the left side of the heatshield, potentially due to the nonzero roll configuration.

B. Flow unsteadiness: Kulites and Schlieren images

While static tap and PSP images provide information about average pressure distributions on the heatshield, flow unsteadiness is an essential factor in vehicle dynamics and control. This unsteadiness was measured via Kulites on the vehicle surface and via Schlieren images of the retropropulsive plumes.

Kulite C_p standard deviations are directly comparable to the temporal unsteadiness measured from CFD. Figure 9 compares the converence of the Kulite and OVERFLOW DES data. Standard deviations were typically ≤ 0.6 for all conditions with $\beta = 0$. As shown in Fig. 10, conditions with nonzero β and/or ϕ indicated much higher unsteadiness levels, especially at high Mach and CT conditions. Kulite data shows that the 2s runtime is generally sufficient to converge C_p means and standard deviations, though some cases show convergence issues due to discontiuities in the instantaneous data. A full list of these discontinuous datasets will be given in the appendix. Present data indicates that similar convergence of kulite C_p running statistics can be achieved in CFD with runtime around 20-40ms.

Schlieren imaging also indicated high levels of unsteadiness in the flow field at either high CT conditions or nonzero roll conditions. In the final paper, DES simlations of these nonzero roll cases will be presented and compared to experimental Schlieren images. An example of instantaneous Schlieren images from the experiment and computed numerically using OVERFLOW DES are given in Fig. 11. The average of the two images may also be compared. Given the importance of the presence of a saddle region between the two main plume banks, these images can also be used in comparisons of the bow shock topology. In the final version of this paper, an assessment of bow shock shape and mean standoff distance will also be given.

C. Effect of turbulence modelling

In static tap, Kulite, and PSP data, OVERFLOW DES calculations generally showed better agreement with experimental data than OVERFLOW URANS calculations, which tends to underpredict experimental C_p values. The difference between URANS and DES is prominent at higher C_T values and displays slight Mach number dependence. Increased C_p values were observed pointwise in the mean tap measurements, unsteady Kulite measurements, and qualitatively in the PSP contours of C_p on the Cobra heatshield. Instantaneous Schlieren images showed greater similarity to instantaneous numerical Schlieren images from DES calculations, and Schlieren movies indicate similar levels of plume unsteadiness and penetration into the freestream flow.

Examples of the OVERFLOW results with various turbulence modelling options compared to experimental data of C_p is given in Fig. 12 and 13. At $M = 3.5$, URANS and DES calculations show vastly different C_p contours on the vehicle's heatshield, with a peculiar 'X'-shaped contour on the URANS solution. At this condition and other $M = 3.5$ conditions, DES is the obvious choice of turbulence model to match experimental data. Conversely, at

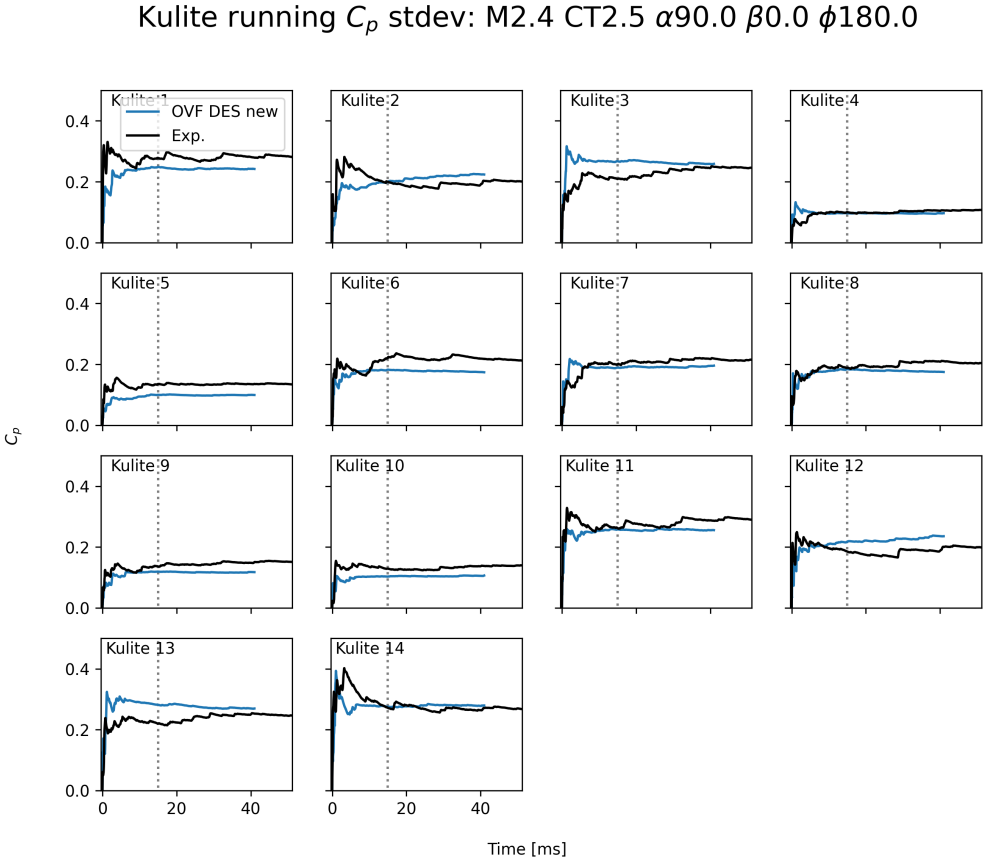

Fig. 9 Standard deviation of experimental and OVERFLOW post-test DES Kulite C_p values at $M = 2.4, \alpha = 90, \beta = 0, \phi = 180, CT = 2.5$. Dashed line at $t = 15ms$ indicates estimated end of DES transience.

$M = 2.4, CT = 2.5, \alpha = 90$, neither URANS nor DES calculations show more favorable agreement with experimental PSP and static tap comparisons. Preliminary TMRC results show the best agreement out of the available results. The final paper will include these results and more detailed flow field comparisons among the turbulence modelling options will be included.

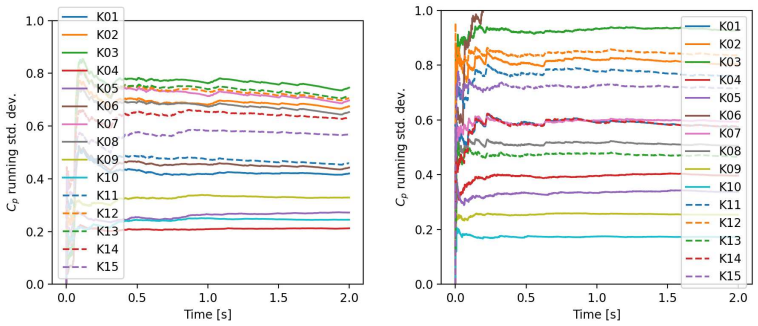

Fig. 10 Standard deviation of experimental Kulite C_p highly unsteady conditions at (left) $M = 2.4, CT = 2.5, \alpha = 90, \beta = 10, \phi = 90$**; (right)** $M = 3.5, CT = 2.5, \alpha = 80, \beta = -5, \phi = 153.4$**.**

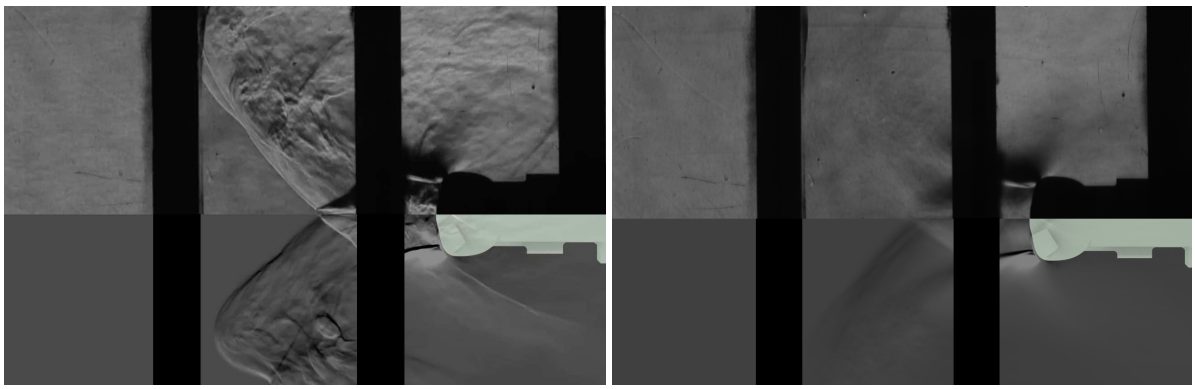

Fig. 11 Experimental schlieren (top) and numerical schlieren of OVERFLOW DES (bottom) calculations at M=3.5, CT=2.5, α=90.

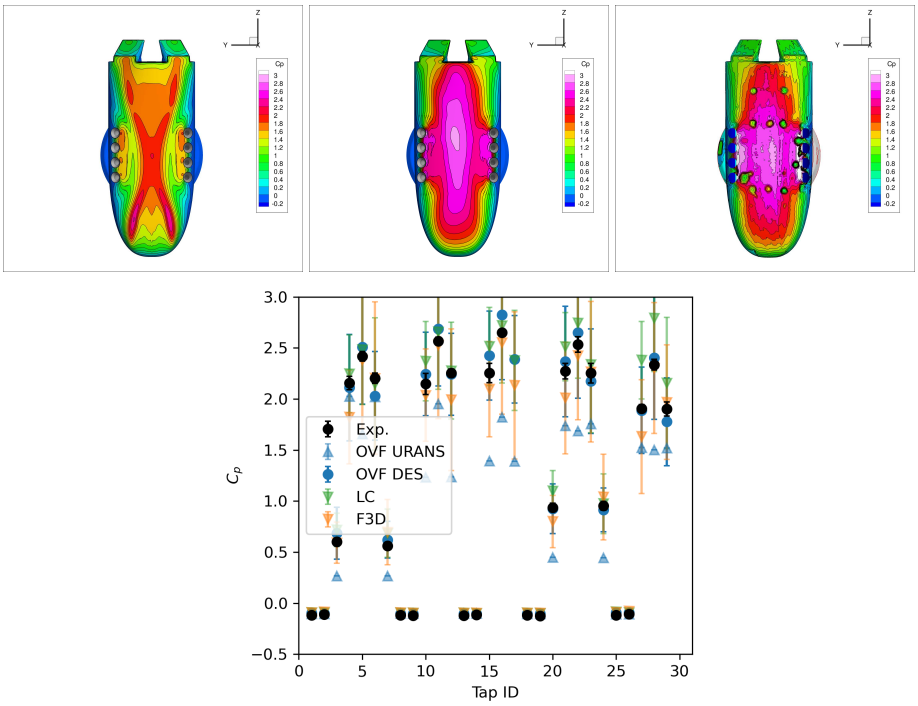

Fig. 12 Comparison of turbulence models' average heatshield C_p contours (left to right: URANS, DES, TMRC, raw PSP) and static tap values at $M = 3.5, CT = 2.5, \alpha = 90$.

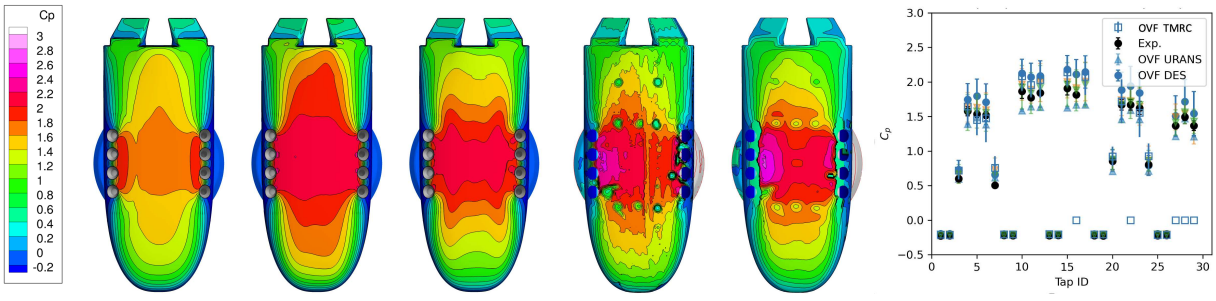

Fig. 13 Comparison of turbulence models' average heatshield C_p contours (left to right: URANS, DES, TMRC, raw PSP, filtered PSP) and static tap values at $M = 2.4, CT = 2.5, \alpha = 90$.

D. Effect of jet boundary condition

A temperature drift (approximately monotonically decreasing) in the plenum of the jets was recorded during the experiment due to difficulty maintaining heated air temperatures. As the experiment was conducted from high to low CT values, this drift become more prominent at lower CT values. In some cases, the difference in temperature between the target (and pre-test CFD) jet plenum temperature was greater than 40 R. Jet pressure were adjusted to obtain the target CT value. Calculations using URANS in OVERFLOW were conducted at M=3.5, CT=1.0, α=90 using pre-test estimates for jet boundary conditions and experimentally measured jet boundary conditions. The latter case has a temperature drift of 45R, which corresponds to a 6.6% decrease in jet total temperature ratio $T_{tj}/T_{t\infty}$ compared to pre-test calculations. The results of this case study indicated that while the drift in temperature gives observable variation in C_p mean values, the variation is small compared to the variation due to turbulence modelling.

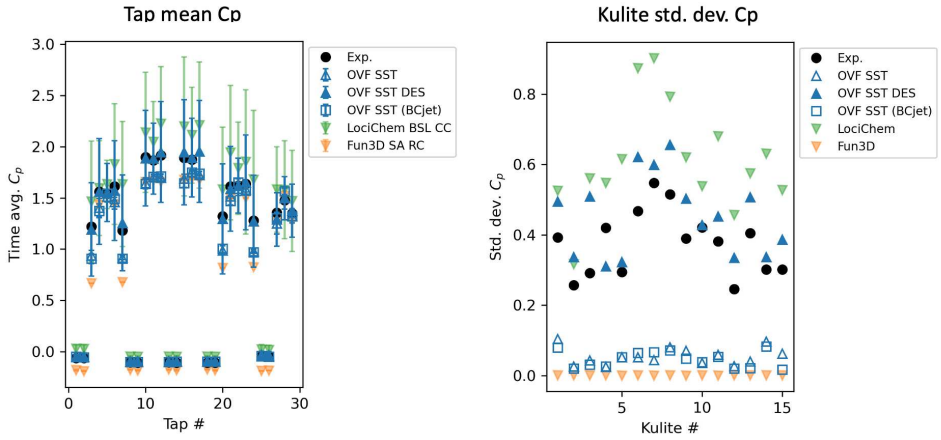

Fig. 14 Experimental and CFD measures of C_p at M=3.5, CT=1.0, α=90. to show the effect of jet boundary conditions is small compared to the effect of turbulence modelling (SST compared to SST DES).

IV. Conclusions and future work

The CobraMRV under SRP conditions experiences complex flow patterns as the vehicle flies though a non-uniform and potentially unsteady flow field created by interactions between the plumes and the bow shock. In this work, the effects of various CFD parameters on these complex flow solutions and vehicle loads is presented. Several flight and engine operating conditions exhibited sensitivity to the choice of turbulence model.

The final paper will include detailed results for post-test cases (cases with no pre-test DES, nonzero beta cases, etc) and documentation of cases with Kulite convergence issues.

Acknowledgments

This work is funded by NASA's Aerosciences Evaluation and Test Capability program office under the Aeronautics Research Mission Directorate. CFD calculations were run on NASA Advanced Supercomputing Division computers. The CFD analysis to date has been funded by the NASA Space Technology Mission Directorate's Game Changing Development Program. The authors thank members of the AETC DSS CFD teams, too numerous to list here, for their advice and review of research, as well as L. Halstrom and S. Lawrence for their reviews of this research.

References

[1] Cerimele, C., Robertson, E., Sostaric, S., Campbell, C., Robinson, P., Matz, D., Stachowiak, S., Garcia, J., Bowles, J., Kinney, D. J., and Theisinger, J., "A Rigid Mid-Lift-to-Drag Ratio Approach to Human Mars Entry, Descent, and Landing," *AIAA SciTech Form 2017*, 2017-1898.

[2] Cianciolo, A. D., Korzun, A., Samareh, J., Sostaric, R., Calderon, D., and Garcia, J., "Human Mars Entry, Descent, and Landing Architecture Study: Phase 3 Summary," *AIAA SciTech Form 2020, Orlando, FL*, 2020-1509.

[3] Edquist, K., Glass, C., Korzun, A., Wood, W., West, T., Alter, S., Canabal, F., Childs, R., Halstrom, L., and Matsuno, K., "Computational Analysis of Two Mars Powered Descent Vehicle Concepts Tested in the Langley Unitary Plan Wind Tunnel," *AIAA Aviation Forum*, 2024.

[4] Halstrom, L., Childs, R., Stremel, P., Garcia, J., and Pulliam, T., "Comparison of OVERFLOW Computational and Experimental Results for a Blunt Mars Entry Vehicle Concept During Supersonic Retropropulsion," *AIAA Aviation Forum*, 2024.

[5] Hollis, B. R., "Real-gas flow properties for NASA Langley Research Center aerothermodynamic facilities complex wind tunnels," Tech. rep., 1996.

[6] Matsuno, K., Halstrom, L., Pulliam, T., Childs, R., Stremel, P., and Garcia, J., "OVERFLOW Guidelines for Simulation of Supersonic Retropropulsion," *AIAA Aviation Forum*, 2024.

[7] Matsuno, K., Childs, R., Pulliam, T., Stremel, P., and Garcia, J., "OVERFLOW Analysis of Supersonic Retropropulsion Testing on the CobraMRV Mars Entry Vehicle Concept," *AIAA SciTech Forum*, 2022.

[8] Menter, F. R., "Two-equation eddy-viscosity turbulence models for engineering applications," *AIAA journal*, Vol. 32, No. 8, 1994, pp. 1598–1605.

[9] Spalart, P. R., "Detached-Eddy Simulation," *Annual Review of Fluid Mechanics*, Vol. 41, No. 1, 2009, pp. 181–202. https://doi.org/10.1146/annurev.fluid.010908.165130, URL https://doi.org/10.1146/annurev.fluid.010908.165130.

[10] Childs, R., and Matsuno, K., "Novel Turbulence Model Tailored for Rocket Motor Exhaust Jets," *AIAA Aviation Forum*, 2024.

[11] Nichols, R., "Algorithm and turbulence model requirements for simulating vortical flows," *46th AIAA Aerospace Sciences Meeting and Exhibit*, 2008, p. 337.

[12] Suzen, Y., and Hoffmann, K., "Investigation of supersonic jet exhaust flow by one-and two-equation turbulence models," *36th AIAA Aerospace Sciences Meeting and Exhibit*, 1998, p. 322.

[13] Spalart, P. R., "Strategies for turbulence modelling and simulations," *International journal of heat and fluid flow*, Vol. 21, No. 3, 2000, pp. 252–263.

[14] Mani, M., Babcock, D., Winkler, C., and Spalart, P., "Predictions of a supersonic turbulent flow in a square duct," *51st AIAA Aerospace Sciences Meeting including the New Horizons Forum and Aerospace Exposition*, 2013, p. 860.